Control of Crystal Structures and Optical Properties with Hybrid Formamidinium and 2-Hydroxyethylammonium Cations for Mesoscopic Carbon-Electrode Tin-Based Perovskite Solar Cells

Cheng-Min Tsai,[†] Yu-Pei Lin,[†] Murali Krishna Pola,[†] Sudhakar Narra,[†] Efat Jokar,[†] Yaw-Wen Yang,[‡] and Eric Wei-Guang Diau*[,†,§]

[†]Department of Applied Chemistry and Institute of Molecular Science, National Chiao Tung University, Hsinchu 30010, Taiwan
[‡]National Synchrotron Radiation Research Center, Hsinchu 30076, Taiwan
[§]Center for Emergent Functional Matter Science, National Chiao Tung University, 1001 Ta-Hsueh Road, Hsinchu 30010, Taiwan

S *Supporting Information*

ABSTRACT: Alcohol-based bifunctional ammonium cations, 2-hydroxyethylammonium (HEA$^+$), HO(CH$_2$)$_2$NH$_3$$^+$, were introduced into formamidinium (FA$^+$) tin-based perovskites (HEA$_x$FA$_{1-x}$SnI$_3$; x = 0−1) to absorb light in carbon-based mesoscopic solar cells. We found that HEA$^+$ cations play a key role to control the crystal structures, the lattice structures altered from orthorhombic (x = 0) to rhombohedral (x = 0.2−0.4) with greater symmetry. When x was increased to 0.6−1.0, tin and iodide vacancies were formed to generate 3D-vacant perovskites (HEA$_x$FA$_{1-x}$Sn$_{0.67}$I$_{2.33}$, $x \geq 0.6$) with a tetragonal structure. Tin-based perovskites in this series were fabricated into mesoporous solar cells using one-step drop-cast (DC), two-step solvent-extraction (SE), and SE + 3% ethylenediammonium diiodide (EDAI$_2$) as an additive. After optimization of device performance with the SE + 3% EDAI$_2$ approach, the HEA$_{0.4}$FA$_{0.6}$SnI$_3$ (HEAI = 40%) device gave the best photovoltaic performance with J_{SC} = 18.52 mA cm^{-2}, V_{OC} = 371 mV, FF = 0.562, and overall efficiency η = 3.9% after the device was stored for a period of 340 h.
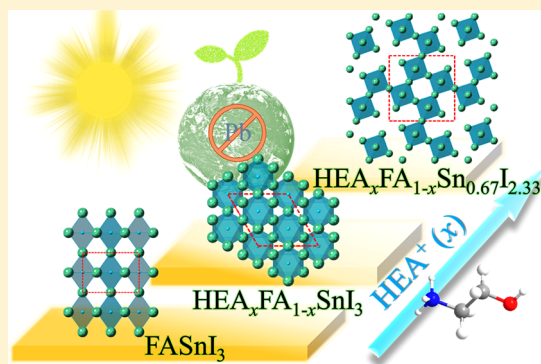
All-solid-state organic−inorganic lead-halide perovskite solar cells (PSCs) have emerged as the most promising next-generation photovoltaic (PV) devices because the efficiencies of power conversion (PCE) of those devices have rapidly increased beyond 22%.[1] PSCs have the advantages of cheap fabrication,[2] versatile configuration, and excellent optoelectronic properties,[3−5] which distinguish PSCs in PV research.[6] Concern arises, however, about conventional perovskite materials containing toxic element lead.[7] As a result, development of lead-free PSCs has become an important issue for future commercialization of PSCs. According to the Shockley−Queisser efficiency limit, the maximum PCE of a single p−n junction PV device under AM 1.5G irradiation can be 33% with a bandgap of ~1.3 eV of the absorber,[8,9] which makes tin-based PSCs a promising candidate for lead-free PSCs. In 2014, Hayase and co-workers applied alloyed Sn/Pb perovskites as light absorbers to partially replace the lead within the perovskite structure and attained a

PCE of 4.2% at a ratio of Sn:Pb = 50:50.[10] Two reports concurrently appeared about methylammonium tin triiodide (MASnI$_3$) PSCs, one from Kanatzidis and co-workers[11] and another from Snaith and co-workers.[12] They showed MASnI$_3$ cells with PCE ≈ 6% and an open-circuit voltage V_{OC} up to ~0.8 V, but the reproducibility of the device performance was poor.[12] There was consequently no report of a mesoscopic regular MASnI$_3$ device with such great device performance until 2017.[13]

The poor reproducibility of a tin-based PSC is attributable to the greater potential levels of the perovskite valence band maximum (VBM)[10,14−17] and the tendency for Sn^{2+} to oxidize to Sn^{4+},[16,18−20] which might result in poor alignment of energy

levels with a hole-transporting material (HTM) and create massive centers of electron–hole recombination, respectively. We have investigated tin-rich perovskites $(MASn_{0.75}Pb_{0.25}I_{3-x}Cl_x)$[15] and trihalide pure tin perovskites $(MASnIBr_{1.8}Cl_{0.2})$[21] with a mesoscopic carbon-based device structure that resulted in device performances of 5.1[15] and 3.1%[21] for the former and the latter devices, respectively. In previous work, we modified the energy levels of a typical ABX_3 perovskite by varying the B and X components to improve the performance and the stability of the device.[15,21] According to literature reports,[22−27] candidates for component A applied to tin-based PSCs were based mostly on Cs^+, MA^+, and FA^+. In 2004, Mercier et al.[28] applied an alcohol-based bifunctional ammonium cation, $HO(CH_2)_2NH_3^+$ (2-hydroxyethylammonium; HEA^+), to stabilize a two-dimensional (2D) perovskite, $(HEA)_2PbI_4$. In the present work, we focused on modification of the energy levels by altering component A upon mixing two organic cations, formamidinium (FA^+) and HEA^+ in varied proportions, to improve the device performance and the stability of a lead-free tin-based PSC.

According to our approach, HEAI and FAI in varied ratios were reacted with SnI_2 in equimolar proportions to synthesize pure tin perovskites with chemical formula $HEA_xFA_{1-x}SnI_3$. As the value of x increased, the crystal structure altered from orthorhombic ($x = 0$) to rhombohedral ($x = 0.2−0.4$) and then to tetragonal ($x = 0.6−1.0$). A 3D-vacant perovskite was produced at $x = 0.6−1.0$. Moreover, when the proportion of HEAI was increased, the bandgap energy also systematically increased from 1.34 eV ($x = 0$) to 2.07 eV ($x = 1$); the VBM systematically altered from −4.91 eV ($x = 0$) to −5.50 eV ($x = 1$). We applied $HEA_xFA_{1-x}SnI_3$ perovskites to fabricate devices with a mesoscopic carbon-electrode structure using a one-step drop-cast (DC) method similar to that applied for a lead-based PSC.[29] We found that the performance of the hybrid $HEA_xFA_{1-x}SnI_3$ devices tripled from PCE 0.8% based on a pristine $FASnI_3$ ($x = 0$) to PCE 2.5% based on a hybrid $HEA_{0.4}FA_{0.6}SnI_3$ ($x = 0.4$); the device performance deteriorated at larger proportions of x (>0.4). A similar approach was reported for a lead-based PSC,[30] but for the lead-based PSC, introducing the HEA^+ cation failed to improve the device performance. In contrast, the performance of the $HEA_{0.4}FA_{0.6}SnI_3$ device improved further with a two-step solvent-extraction (SE) method[31] with cosolvent DMF:DMSO = 50:50 to attain PCE 3.0%; the device performance was optimized to PCE 3.7% upon adding ethylenediammonium diiodide (EDAI$_2$ 3%) in trace proportion.[32]

$HEA_xFA_{1-x}SnI_3$ ($x = 0−1$) perovskites were synthesized upon mixing HEAI/FAI and SnI_2 precursors in equimolar proportions in DMF (Figure 1); ratios of HEA^+:FA^+ were controlled upon varying the HEAI:FAI proportions with molar ratios 0:100, 20:80, 40:60, 60:40, 80:20, and 100:0, which correspond to fractions of organic cations $x = 0$, 0.2, 0.4, 0.6, 0.8, and 1, respectively. Figure 1 shows the chemical equations for the formation of hybrid perovskites $HEA_xFA_{1-x}SnI_3$ according to a stoichiometric condition. The absorption and photoluminescence (PL) spectra of perovskites of this series deposited on mesoporous Al_2O_3/glass substrates were recorded to derive the optical properties of these perovskite crystals inside of a mesoporous condition to mimic the environment in a mesoscopic carbon-electrode device (Figure 1). Increasing the proportions of HEAI in perovskites evidently shifted the absorption spectra toward smaller wavelengths; for band edges varying from 925 nm ($x = 0$) to 614 nm ($x = 1$),
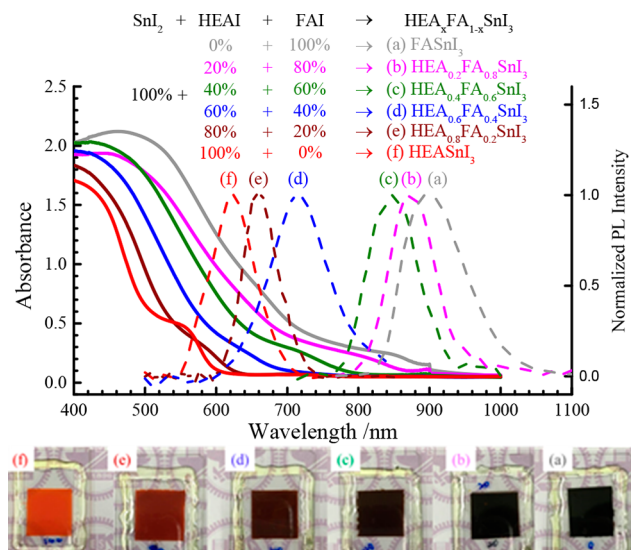

Figure 1. Absorption (solid curves) and normalized PL (dashed curves) spectra of $HEA_xFA_{1-x}SnI_3$ films deposited on mesoporous Al_2O_3/glass substrates with varied HEAI:FAI ratios ($x = 0−1$) controlled by stoichiometric proportions of HEAI:FAI precursors. Chemical equations (a−f) appear above the spectra and the corresponding photographs of thin-film samples below the spectra.

the corresponding normalized PL spectra shifted from 900 nm ($x = 0$) to 623 nm ($x = 1$); the films changed accordingly from black to orange (Figure 1). The systematic variation of the absorption and PL spectra provide importants information regarding the variation of the bandgap (E_g) of the hybrid cation perovskites; we hence expect that the HEA^+ cation plays a key role to modify the crystal structures for the observed variation of the bandgaps in tin-based perovskites in this series.

Figure 2a shows X-ray diffraction (XRD) patterns of $HEA_xFA_{1-x}SnI_3$ perovskites deposited on FTO/TiO$_2$/Al$_2$O$_3$/C device substrates with $x = 0$, 0.2, 0.4, 0.6, 0.8, and 1; Figure 2b shows powder XRD patterns extracted from four new single-crystal data with the crystal structures shown in Figure 2 panel c (HEAI 40 and 80%, 3D structure) and panel d (HEAI 100%, 2D structure). As shown in Figure 2a, all diffraction signals shift toward smaller diffraction angles as the HEAI proportion increases, meaning that HEA^+ cations are involved during formation of the perovskite crystals; this phenomenon reasonably explains the variation of bandgaps of perovskites of this series shown in Figure 1. As HEA^+ is larger than FA^+, the crystal size would increase with increasing number of inserted HEA^+ cations, resulting in downward shifts of the diffraction angles. The intensities of diffraction signals at 14.2 and 28.4° consistently increased with increasing proportion of HEA^+, indicating that the crystallinity of the perovskite crystals improved with HEA^+ incorporated into the crystals. As the HEAI proportion increased to 40%, the intensities of XRD signals at 14.2 and 28.4° attained maxima; the intensity of the diffraction signal at 14.2° was greater than that at 24.6°, in contrast with the HEAI 0% sample. These phenomena indicate that the crystal structures of $HEA_xFA_{1-x}SnI_3$ perovskites alter upon increasing x. As the proportion of HEAI increased to 60%, the patterns of the XRD signals at 14.2, 28.4, 31.8, 40.5, and 43.1° altered from singlet to doublet. When the proportion of HEAI increased to 80 and 100%, not only did the doublet nature become more pronounced but also two additional diffraction signals appeared at 6.0 and 8.5°, marked # in Figure
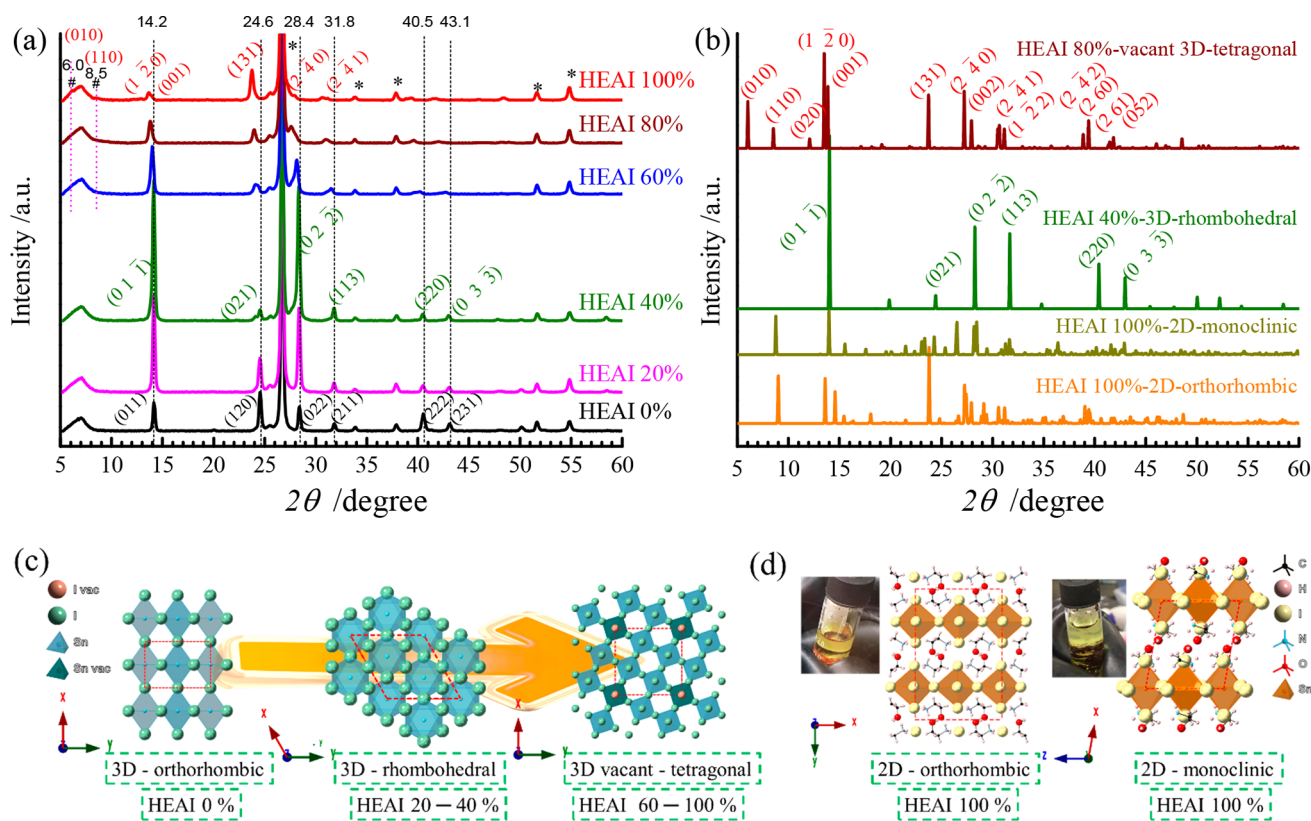
Figure 2. (a) XRD patterns of HEA$_x$FA$_{1-x}$SnI$_3$ perovskites deposited on mesoporous FTO/TiO$_2$/Al$_2$O$_3$/C device substrates with varied HEAI:FAI ratios as indicated. The intense XRD signals marked * correspond to a contribution from the carbon layer and the FTO substrate; small diffraction patterns at 6.0 and 8.5° are marked #. (b) Powder XRD patterns of HEA$_x$FA$_{1-x}$SnI$_3$ single crystals obtained by analyzing four new single-crystal structures shown in (c) and (d). (c) Kinetic preferred perovskite structures of single crystals with HEAI proportions 0, 40, and 80% represented from left to right. The corresponding XRD patterns shown in the top two traces of (b) for HEAI 40% and HEAI 80% single crystals were transferred from their corresponding CIF files. (d) Thermodynamically preferred crystal structures obtained from two HEAI 100% single crystals show the 2D structural feature. The corresponding XRD patterns shown in the bottom two traces of (b) for HEAI 100% single crystals of two types were transferred from their corresponding CIF files.

Table 1. Lattice Parameters of HEA$_x$FA$_{1-x}$SnI$_3$ Perovskites Obtained from TOPAS Simulations at Varied Proportions of HEAI as Fitted Results Shown in Figure S2, SI^a

crystal type	HEAI proportion/%	crystal geometry	space group	a/Å	b/Å	c/Å	α/deg	β/deg	γ/deg
powder sample	0	orthorhombic	$Amm2$	6.3164(7)	8.9506(28)	8.9432(14)	90	90	90
	20	rhombohedral	$R3$	8.9130(6)	8.9130(6)	10.9133(17)	90	90	120
	40	rhombohedral	$R3$	8.9242(8)	8.9242(8)	10.9247(8)	90	90	120
	60	tetragonal	$P4/m$	14.559(3)	14.559(3)	6.3765(16)	90	90	90
	80	tetragonal	$P4/m$	14.637(3)	14.637(3)	6.381(2)	90	90	90
	100	tetragonal	$P4/m$	14.6706(7)	14.6706(7)	6.3852(5)	90	90	90
single crystal	40^b	rhombohedral	$R3$	8.920(4)	8.920(4)	10.934(4)	90	90	120
	80^b	tetragonal	$P4/m$	14.620(9)	14.620(9)	6.392(4)	90	90	90
	100^c	orthorhombic	$Pnma$	13.0062(18)	19.617(4)	6.3852(13)	90	90	90
	100^c	monoclinic	$P2_1/c$	10.1959(2)	9.0234(2)	8.9297(2)	90	100.360(1)	90

^{a}The lattice parameters in the lower part of the table were obtained from the single-crystal data. ^{b}Extracted from single-crystal data with a 3D structure. ^{c}extracted from single-crystal data with a 2D structure.

2a; the same feature was observed in the powder XRD patterns shown in Figure S1, SI.

To provide further information about the variation of the diffraction patterns and to understand the transfer of the crystal phases, we prepared both powder samples and single crystals with a sealed-tube method and a method involving slow cooling of the solution (or solution−vapor), respectively. We can see clearly the new signals from the powder diffraction data of the sealed-tube HEA$_x$FA$_{1-x}$SnI$_3$ powder samples shown

in Figure S1, SI. Three new diffraction signals emerged at 6.0, 8.5, and 12.1°; five diffraction signals aforementioned became more split when the HEAI:FAI ratios increased to 60:40 and above, which are important features similar to those of the device samples shown in Figure 2a. The simulated TOPAS results of these powder samples appear in Figure S2, SI; the corresponding lattice parameters are summarized in Table 1. The TOPAS results reveal that the crystal geometry and space group of the perovskite unit cells transferred from

orthorhombic *Amm*2 of lower symmetry to rhombohedral *R*3 of higher symmetry when the proportion of HEAI increased from 0 to 20−40%. This structural variation indicates that HEA$^+$ cations insert into the perovskite lattice and increase the symmetry order of a crystal. We therefore grew single crystals of HEA$_{0.4}$FA$_{0.6}$SnI$_3$ perovskite with a slow-cooling method; the obtained crystal structure is shown in the middle of Figure 2c. Because of thermal vibrations of the mixed organic cations, only the inorganic network was located; both organic cations could not be revealed from the matrix of small electronic density. The crystal structure altered again when the proportion of HEAI increased to 60−100%. The single crystal of the HEA$_{0.8}$FA$_{0.2}$ Sn$_{0.67}$I$_{2.33}$ perovskite, prepared with a solution−vapor method, adopts a tetragonal structure but with vacancy sites of tin and iodine, which we call a *vacant perovskite*, with the structure of the unit cell shown in Figure 2c right. On the basis of the single-crystal structure of a perovskite with HEAI 80%, both lattice parameters of the HEAI 60 and 100% crystals were determined unambiguously from a TOPAS simulation of the corresponding powder data according to the results summarized in Table 1; they all belong to the category of 3D-vacant perovskites with the same tetragonal lattice structure *P*4/*m* with size increasing with increasing proportion of HEAI.

When the perovskite crystal with the HEAI proportion increases from 40 to 60%, why does a phase transition occur to generate a 3D-vacant structure? Because the size of HEA$^+$ is much greater than that of FA$^+$, the crystals of greater HEAI proportion might suffer from a large structural stress that requires release. One way to release such crystal strain is for tin and iodine ions to escape from the crystal so that structural vacancies emerge. As a result, the structural motif enlarged; both *a* and *b* of the unit cells increased from 8.920 to 14.559 Å (Table 1). The single-crystal structure shown in Figure 2c indicates that tin and iodine vacancies posited at corner sites of the unit cell with an inorganic frame Sn$_4$I$_{14}$. The 3D-vacant perovskites can thus be regarded as bridging between a 2D and a 3D structure, giving the 3D-vacant perovskite molecular formulas HEA$_x$FA$_{1−x}$Sn$_{0.67}$I$_{2.33}$. A similar phenomenon was found in the case of lead perovskite reported by Mercier et al.,[30] who applied HEA$^+$ to MAPbI$_3$ perovskites to form vacant perovskite with inorganic crystal frame Pb$_{4.09}$I$_{14.09}$, which is similar to our case with inorganic frame Sn$_4$I$_{14}$. For the case of tin perovskite, Kanatzidis and co-workers added ethylenediamine (en) in small proportions into FASnI$_3$ and MASnI$_3$ to form so-called *hollow perovskites* {en}FASnI$_3$ and {en}-MASnI$_3$.[25,26] As en^{2+} (or EDA^{2+}) cations are involved, Sn^{2+} must emerge from the crystal lattice to maintain a charge balance, which might thus generate Schottky vacancies in massive numbers. Their vacancy sites are randomly occupied, which differs from our case.

In 2004, Mercier et al. reported two 2D lead-based perovskites, HEA$_2$PbI$_4$ and HEA$_2$PbBr$_4$, of which the unit cells have monoclinic and orthorhombic structures, respectively.[28] Using a slow-cooling method, we synthesized single crystals of 2D tin-based perovskite HEA$_2$SnI$_4$; the precursor solution contained HEAI 100%. Differing from the case of HEA$_2$PbI$_4$, the HEA$_2$SnI$_4$ crystallized near 25 °C to form lattice structures monoclinic (*P*21/*c*) and orthorhombic (*Pnma*), showing dark brown and orange colors, respectively. In the two unit cell structures shown in Figure 2d, the SnI$_6$ octahedral inorganic framework was separated by the HEA$^+$ cations. Because the interaction between each inorganic layer

was small, the two HEA$_2$SnI$_4$ perovskites all had a sheet-like morphology. In contrast, when the precursor solution with HEAI 100% was used either with the DC method to make a device or with a sealed-tube method to make a powder sample, only 3D-vacant perovskites were produced, as the preceding discussion shows. This discrepancy might be due to two distinct crystal growths involved. For the case with the DC and sealed-tube method, the crystal growth was so rapid that the crystal was generated in a kinetically preferable phase, a 3D-vacant perovskite, rather than its thermodynamically preferable phase, a 2D perovskite, which was produced with the slow-cooling method aforementioned.

Our XRD results indicate three important structural features of the HEA$_x$FA$_{1−x}$SnI$_3$ perovskites. First, introducing HEA$^+$ increases the order of the lattice symmetry at *x* = 0.2−0.4 (HEAI 20−40%) to expand the unit cell with a 3D rhombohedral structure (symmetry *R*3). Second, the crystal structure transfers from a 3D perovskite structure to a 3D-vacant perovskite structure at *x* = 0.6−1.0 (HEAI 60−100%) with general chemical formula HEA$_x$FA$_{1−x}$Sn$_{0.67}$I$_{2.33}$ adopting a tetragonal structure with a larger unit cell. Third, for the HEAI 100% case, the 3D-vacant perovskites (HEASn$_{0.67}$I$_{2.33}$) are in a kinetically preferable phase and the 2D perovskites are in a thermodynamically preferable phase. We thus discovered that HEA$^+$ cations play an important role within the HEA$_x$FA$_{1−x}$SnI$_3$ perovskite framework, which altered the crystal structure; this structural alteration has an impact on the optical, electronic, and PV properties of the materials, as we discuss in what follows.

The energy levels of the valence band (E_{VB}) of perovskite system HEA$_x$FA$_{1−x}$SnI$_3$ were investigated with ultraviolet photoelectron spectra (UPS) and photons at energy 36.4 eV from a synchrotron radiation source in an ultrahigh vacuum system. The photoelectron kinetic energies and binding energies were determined from the two edges of the UPS to obtain E_{VB} for the HEA$_x$FA$_{1−x}$SnI$_3$ perovskites. The small-energy edge shows the work function (WF); the large-energy edge determines the energy difference between the WF and VBM; the corresponding UPS raw data and analysis are shown in Figures S3, SI. The energy levels of the minimum of the conduction band (CBM, E_{CB}) were determined upon scaling the VBM levels with the corresponding E_g values, which were determined from the absorption spectra shown in Figure S4, SI. Figure 3a shows energy levels (VBM and CBM) and the WF for perovskites HEA$_x$FA$_{1−x}$SnI$_3$ with precursor solutions containing HEAI/FAI in varied proportions. For FASnI$_3$ (*x* = 0), the WF is located at −4.21 eV and the VBM is at −4.91 eV. When HEA$^+$ was introduced, both the WF and VBM energy levels were systematically lowered from −4.24 and −5.19 eV at *x* = 0.2 to −4.34 and −5.50 eV at *x* = 1.0. In contrast, the CBM energy levels were lowered from −3.57 eV at *x* = 0 to −3.76 eV at *x* = 0.4 and then systematically raised to −3.43 eV at *x* = 1.0. The lowest CBM of the HEA$_x$FA$_{1−x}$SnI$_3$ perovskites is located at *x* = 0.4. The energy gap between the CBM and WF was also altered radically; it narrowed from *x* = 0 to 0.4 and then expanded from *x* = 0.4 to 1.0, similar to the trend of variation of the CBM. Figure 3b shows the variations of both the WF and the energy gaps between the CBM and WF. From *x* = 0.4 to 0.6, a large decrease of the WF was observed because a phase transition occurred to form a 3D-vacant perovskite at *x* ≥ 0.6, which led to significantly altered E_g and the correspondingly altered energy levels shown in Figure 3a. The hybrid cation perovskite at *x* = 0.4 hence shows the
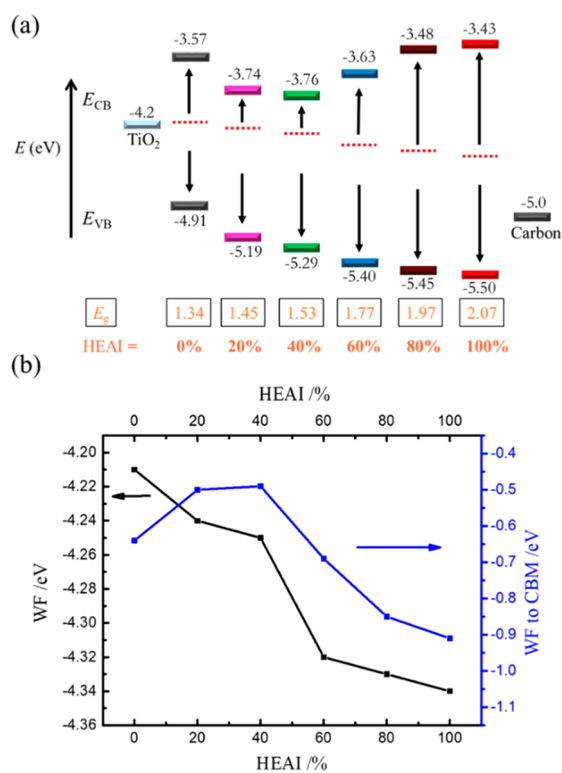
Figure 3. (a) Potential energy diagrams (energy/eV with respect to vacuum) of films HEA$_x$FA$_{1-x}$SnI$_3$ with the percentage of HEAI in the HEAI:FAI film as indicated. E_{VB} and E_{CB} represent the potential levels of the VBM and CBM, respectively; E_g represents the energy bandgap; the positions of the WF are indicated as red dashed lines for each species. (b) Trend of the WF (left axis) and the energy difference between the WF and CBM (right axis) of varied HEA proportions. The raw data of the UPS are shown in Figure S3, SI.

narrowest energy gap between the CBM and WF, 0.49 eV, indicating a stronger n-type behavior for HEA$_{0.4}$FA$_{0.6}$SnI$_3$ than that for other hybrid perovskites. These results illustrate the capability of energy-level modification with varied proportions of HEAI precursor, for which the sample at HEAI 40% features a strong n-type characteristic to match the E_{CB} of TiO$_2$ for feasible electron transfer from perovskite to the TiO$_2$ layer.

The VBM and CBM of the ABX$_3$ perovskites are reported to be dominated by hybridized p-orbitals of X anions interacting with s- and p-orbitals of B cations, respectively.[33−37] The cation A seems not to contribute directly to the band structure but would contract or tilt the lattice structure so as to affect the distance of the B−X bond; cation A might hence be regarded as an indirect contribution to the variation of the VBM and CBM positions.[33,37] Upon replacing MA$^+$ with FA$^+$ or Cs$^+$, E_g values in perovskites vary within 0.3 eV,[37] whereas by replacing site A cation with a cation of a longer alkyl chain or bifunctional cation, such as butylammonium (BA$^+$)[27] or phenylethyleneammonium (PEA$^+$),[23,24] the crystal structure could alter from 3D to 2D or form a hollow perovskite. As a result, the ability to tune the bandgap can be improved to more than 0.6 eV. In our case, for HEA$_x$FA$_{1-x}$SnI$_3$, the variation of E_g systematically increased to 0.73 eV for perovskites from x = 0 to 1 (Figures 1 and S4, SI). We consider this anomalous alteration of the band structure to be due to the altered crystal structure and symmetry; the unit cells of the perovskite crystals alter from 3D orthorhombic (HEAI 0%) to 3D rhombohedral

(HEAI 20−40%) and then to 3D-vacant tetragonal (HEAI 60−100%). A variation of the band structure of this kind that occurs in our hybrid cation perovskite system because of a phase transition of the crystal structure has not been reported elsewhere.

The HEA$_x$FA$_{1-x}$SnI$_3$ mesoscopic carbon-electrode solar cells were fabricated with precursor solutions containing HEAI/FAI in varied proportions using the DC method according to a procedure reported elsewhere.[29] The side-view SEM images shown in Figure S5, SI, indicate that compact and dense perovskite crystals were uniformly produced and effectively filled inside of the mesoporous pores of the TiO$_2$ and Al$_2$O$_3$ layers. The current−voltage characteristics of the HEA$_x$FA$_{1-x}$SnI$_3$ perovskite devices were measured under 1 sun AM 1.5G irradiation; the results appear in Figures 4a; the

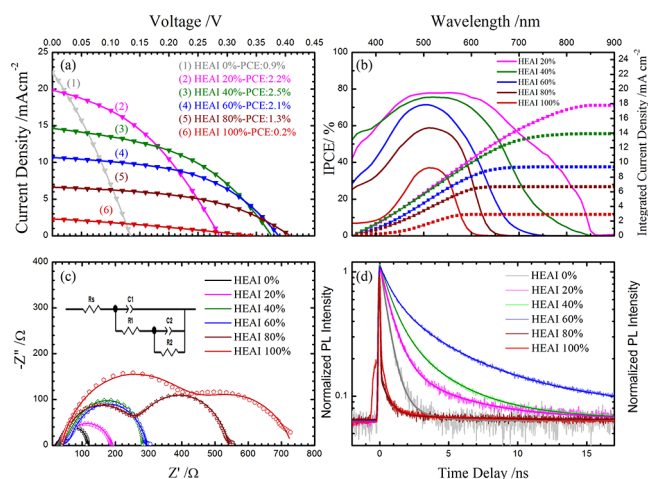Figure 4. PV performance of HEA$_x$FA$_{1-x}$SnI$_3$ devices showing (a) current−voltage curves, (b) IPCE spectra (solid curves) and integrated current densities (symbols), (c) EIS analysis of each condition (symbols are experimental data, fitted data are shown as lines, and the fitted circuit is inserted at the left corner), and (d) PL decays of HEA$_x$FA$_{1-x}$SnI$_3$ deposited on a glass substrate.

corresponding PV parameters are summarized in Table S1, SI. The corresponding spectra of the efficiency of conversion of the incident monochromatic photons to current (IPCE) of each cell are illustrated in Figure 4b. For reference cell HEAI 0%, we obtained no IPCE curve because of its poor stability in air. The integrated current densities of the other cells (Figure 4b) match well their corresponding J−V data (Figure 4a). The short-circuit current density (J_{SC}) shows a trend of systematic decrease from HEAI 0 to 100%, which is consistent with the trend of E_g shown in Figure 3a. In contrast, V_{OC} shows an opposite trend compared with that of J_{SC} with an exception that the HEAI 100% device shows a smaller V_{OC} than the HEAI 80% cell. The abnormal V_{OC} decrease for the HEAI 100% device might be due to the poor n-type characteristic of the perovskite so that charge recombination becomes a serious problem. As shown in Figure 3, the WF position of the HEAI 100% film is located at nearly the midpoint between energy levels E_{CB} and E_{VB}; the gap between the WF and CBM would thus be too large for efficient charge transfer, resulting in decreased V_{OC} and a poor fill factor (FF). The devices show a trend of performance consistent with the variation of the WF to CBM energy gaps shown in Figure 3b; the best PV performance occurred at the HEAI 40% device (PCE 2.5%) for which the WF to CBM energy gap is the least. Moreover, the

HEAI 40% device has the least E_{CB} so as to achieve the best band alignment with E_{CB} of TiO$_2$.

To study the interfacial properties for improved understanding of the trend of device performance shown in Figure 4a, we measured electrochemical impedance spectra (EIS) of HEA$_x$FA$_{1-x}$SnI$_3$ devices with $x = 0-1$; the results are shown in Figure 4c. Nyquist plots of all devices show two arcs that were fitted according to the equivalent-circuit model represented above the plots; the corresponding fitted parameters are listed in Table S2, SI. The two arcs of the Nyquist plots have been assigned to the impedance representing the charge transfer (in the high-frequency region) and charge recombination (in the low-frequency region) behavior of interfaces of the devices.[15,21,38] According to the fitted results summarized in Table S2, SI, the values of both charge-transfer resistance (R_1) and charge-recombination resistance (R_2) show an increasing trend with increasing proportion of HEAI. This feature is consistent with the increasing trend of J_{SC} and decreasing trend of V_{OC} shown in Figure 4a, with an exception of the HEAI 100% device. This exceptional case can be rationalized as the R_2 value of the HEAI 100% device is smaller than the R_1 value. The HEAI 100% device hence suffers from serious charge recombination because the rate of charge transfer would become smaller than the rate of charge recombination. We also notice that there is a large jump for the R_1 values from the HEAI 60% device to the HEAI 80% device, which reflects their corresponding J_{SC} values. Because these two perovskites both exhibit a 3D-vacant structure, the observed abruptly increasing charge-transfer resistance might be due to the defects of the perovskite becoming more significant when more defect states were produced for the HEAI 80% perovskite than for the HEAI 60% perovskite. As a result, the HEAI 40% device with a rhombohedral crystal structure could balance both charge transfer and charge recombination to give the best performance for perovskites in this series.

To evaluate the PL lifetimes, we performed time-correlated single-photon counting (TCSPC) experiments for HEA$_x$FA$_{1-x}$SnI$_3$ samples as thin films. As indicated in Figure 4d, the trend of the PL lifetimes shows the order for HEAI 60 > 40 > 20 > 0 > 80 ≈ 100%. For the reference FASnI$_3$ (0%) sample, only two decay components sufficed for the fit; the first decay component ($\tau_1 = 0.51$ ns) corresponds to a nonradiative surface-state relaxation of perovskite, whereas the second decay component ($\tau_2 = 1.6$ ns) is attributed to charge recombination in the bulk.[39,40] For other samples ($x > 0$), three decay components were required to obtain a satisfactory fit, but for samples from HEAI 20, 80, and 100%, the third component was too small to be included in a calculation of the average PL lifetime (τ_{PL}). We found that τ_1 increased systematically from $x = 0$ to 0.6 and then decreased to a pulse-limited value for $x = 0.8$ and 1.0. This lifetime behavior is consistent with the EIS results (Figure 4c) that show an abruptly increased charge-transfer resistance (R_1) from the $x = 0.6$ to 0.8 devices. The amplitude of τ_1 also showed a systematically decreasing trend from $x = 0$ to 0.6, indicating that the nonradiative surface-state relaxation became less significant when the HEAI proportion increased to 60%, at which the phase transition occurred to form a 3D-vacant perovskite. In contrast, the bulk charge recombination (τ_2) became more important upon increasing the HEAI proportion to 60%. As a result, the trend of average PL lifetime (τ_{PL}) shows an order with HEAI proportion 60 > 40 > 20 > 0 ≫ 80 ≈ 100%. The PL transients of both 80 and 100% samples showed a pulse-limited kinetic feature because

the tin and iodine vacancies inside of the perovskite crystals generated too many defect states to induce significant charge recombination on the surface and in the bulk. Although the 60% sample shows the largest PL lifetime, the existence of vacancies in a small proportion inside of the perovskite made the device performance of the HEA$_{0.6}$FA$_{0.4}$SnI$_3$ cell slightly worse than that of the HEA$_{0.4}$FA$_{0.6}$SnI$_3$ device, shown in Figure 4a and Table S1, SI. We hence take the HEA$_{0.4}$FA$_{0.6}$SnI$_3$ device as a reference cell using varied approaches to optimize its PV performance, as detailed in what follows.

To optimize the device performance for the HEA$_{0.4}$FA$_{0.6}$SnI$_3$ (HEAI 40%) device, we applied a two-step SE method.[31] We found that the crystal growth rate of the perovskite was controllable with the SE method and precursor solvents containing DMF/DMSO in varied proportions. As the results show in Figure S6 and Table S4, SI, the best device performance occurred at the ratio DMF:DMSO = 50:50 (PCE 3.0%), which is superior to that using a one-step DC method with the precursor solvent using DMF 100% (PCE 2.5%). Although the device fabricated using the SE method showed a better J_{SC} and FF than those using the DC method, the V_{OC} was poorer. To improve the cell performance for the SE device, we added EDAI$_2$ in a small proportion, which has been applied to enhance V_{OC} effectively for a planar tin-based PSC.[32] EDAI$_2$ was added into the HEAI 40% precursor solution with the EDAI$_2$ proportions varied from 0 to 5%. The PV performance results are shown in Figure S7 and Table S5, SI; the best device performance occurred at 3% EDAI$_2$. According to this approach (SE + 3% EDAI$_2$), the cell performance was significantly improved, giving the best device with $J_{SC} = 17.20$ mA cm^{-2}, $V_{OC} = 383$ mV, FF = 0.56, and overall efficiency $\eta = 3.7$%. A comparison of the device performance with three methods was made for the best devices (Figure 5a); the corresponding histograms based on 30 devices are shown in Figure 5b. The corresponding PV performance parameters are summarized in Tables 2 and S6–S8, SI. Figure 5c,d shows the effect of hysteresis and stabilized power output, respectively.

The enduring stability tests of the HEAI 0% device (as a reference cell) and the HEAI 40% devices fabricated with three
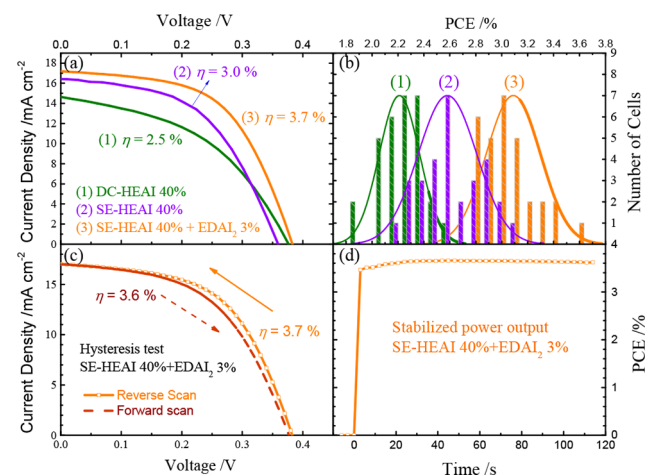

Figure 5. (a) Current–voltage curves and (b) histograms of 30 fresh HEAI 40% devices fabricated using approaches of DC, SE, and SE + 3% EDAI$_2$ additive, (c) hysteresis test of the SE + 3% EDAI$_2$ cell, and (d) stabilized power output measured at the point of maximum power of the SE + 3% EDAI$_2$ device for 2 min.

Table 2. PV Parameters of Carbon-Electrode HEA$_{0.4}$FA$_{0.6}$SnI$_3$ Perovskite Devices Obtained from Current−Voltage Curves Shown in Figure 5a,b

devices		J_{SC}/mA cm^{-2}	V_{OC}/mV	FF	PCE/%
DC[a]	average	14.21 ± 1.36	352 ± 10	0.44 ± 0.03	2.2 ± 0.16
	best	14.67	378	0.45	2.5
SE[b]	average	15.39 ± 1.01	349 ± 18	0.48 ± 0.03	2.6 ± 0.23
	best	16.42	359	0.51	3.0
SE + EDAI$_2$ 3%	average	15.83 ± 0.81	387 ± 13	0.51 ± 0.02	3.1 ± 0.21
	best[c]	18.52	371	0.56	3.9

[a]Perovskite layer made with a one-step DC method. [b]Perovskite layer made with a SE method. [c]After storage in a glovebox for 340 h.

different methods as a function of storage time are demonstrated in Figure S8, SI. Both HEAI 0 and 40% devices fabricated by the DC method showed significant deterioration of the device performance as a function of storage periods. For the HEAI 40%-SE device, the PCE increased slightly and maintained above 2.5% for over 1000 h. For the HEAI 40%-SE + 3% EDAI$_2$ device, we found that the performance of the fresh cell exhibited only PCE 3.2%; the efficiency was slowly increased upon increasing the storage period, and a maximum performance was obtained at a storage time of 340 h, for which J_{SC} = 18.52 mA cm^{-2}, V_{OC} = 371 mV, FF = 0.56, and the overall efficiency η = 3.9%. The diammonium cation, EDA^{2+}, clearly plays an important role in passivating the defect states, suppressing the Sn^{2+}/Sn^{4+} oxidation, and releasing the crystal strain, not only for planar tin-based PSC[32] but also boosting the device performance for our carbon-electrode hybrid organic cationic tin-based PSCs.

In conclusion, we have developed tin-based perovskites in a new series, HEA$_x$FA$_{1-x}$SnI$_3$ (x = 0−1), using precursor solutions containing tin iodide and 2-hydroxyethylammonium iodide/formamidinium iodide (HEAI/FAI) mixtures in varied stoichiometric ratios, 0:100, 20:80, 40:60, 60:40, 80:20, and 100:0. Bifunctional cation HEA$^+$, HO(CH$_2$)$_2$NH$_3$$^+$, exerted vital influence on the structural, optical, and electronic properties of a tin-based perovskite. When HEA$^+$ inserted into the lattice structure, the ordinary crystal symmetry of HEA$_x$FA$_{1-x}$SnI$_3$ increased; the crystal structures altered from orthorhombic (x = 0) to rhombohedral (x = 0.2 and 0.4). When x increased to 0.6−1.0, 3D-vacant perovskites, HEA$_x$FA$_{1-x}$Sn$_{0.67}$I$_{2.33}$, were formed. This 3D-vacant perovskite can be regarded as a structure bridging between 2D and 3D perovskites. As the HEAI proportion increased to 100%, the crystal structures existed in two stable phases, the kinetically preferable phase (HEASn$_{0.67}$I$_{2.33}$) and the thermodynamically preferable phase (HEA$_2$SnI$_4$), which can be controlled by varying the rates of crystal growth. The structural changes of the perovskite crystals led to significant changes in the optical properties, such as bandgaps, and electronic structures, such as band energy levels, which play a key role in PV performance. We applied perovskite HEA$_x$FA$_{1-x}$SnI$_3$ as a light-harvesting active layer to fabricate the mesoscopic carbon-electrode devices. We found that J_{SC} decreased when V_{OC} increased upon increasing the HEAI proportions. The best-performing cell occurred at HEAI 40% (x = 0.4) because of the superior crystallinity, energy level alignment, and retarded charge recombination, supported by the characterization using XRD, UPS, EIS, and TCSPC techniques. The PCE of the HEA$_{0.4}$FA$_{0.6}$SnI$_3$ device was further optimized with a two-step SE method and additive EDAI$_2$ present at 3%, which attained the best efficiency of η = 3.7% for a fresh cell and η = 3.9% for the device stored in a glovebox for 340 h. The present

work conveys an important message that the hybrid HEA$^+$/FA$^+$ organic cations can modify the optoelectronic properties and band structures by altering the lattice structures with varied HEAI proportions. The discovery of new 3D-vacant and 2D tin-based perovskites thus opens a new door for further development of a lead-free perovskite with superior alignment of energy levels and improved performance as a solar cell.

■ ASSOCIATED CONTENT

Ⓢ Supporting Information

The Supporting Information is available free of charge on the ACS Publications website at DOI: 10.1021/acsenergylett.8b01046.

> Photovoltaic parameters, EIS fitted data, fitted PL decay data, powder XRD fitted with TOPAS, UPS, absorption spectra, SEM images, and J−V curves (PDF)
> Crystallographic details and checkCIF/PLATON report for HEA$_{0.4}$FA$_{0.6}$SnI$_3$−FA$_{0.6}$ (ZIP)
> Crystallographic details and checkCIF/PLATON report for HEA$_x$FA$_{1-x}$Sn$_{0.67}$I$_{2.33}$ (ZIP)
> Crystallographic details and checkCIF/PLATON report for HEA$_2$SnI$_4$-monoclinic (ZIP)
> Crystallographic details and checkCIF/PLATON report for HEA$_2$SnI$_4$-orthorhombic (ZIP)

■ AUTHOR INFORMATION

Corresponding Author
*E-mail: diau@mail.nctu.edu.tw.

ORCID Ⓞ
Eric Wei-Guang Diau: 0000-0001-6113-5679

Author Contributions

E.W.-G.D. and C.-M.T. conceived the concept of this work; Y.-P.L. and M.K.P. prepared the materials, fabricated, and characterized the device performance; C.-M.T. conducted the experiments of powder XRD, single-crystal XRD and EIS and analyzed the corresponding results; C.-M.T. and Y.-P.L. carried out UPS experiments and discussed with Y.-W.Y.; S.N. measured steady-state PL and transient PL decays and analyzed the corresponding results; E.J., C.-M.T., and E.W.-G.D. discussed the results; C.-M.T. prepared the initial draft, and E.W.-G.D. wrote the final manuscript.

Notes
The authors declare no competing financial interest.

■ ACKNOWLEDGMENTS

■ REFERENCES

(1) Yang, W. S.; Park, B.-W.; Jung, E. H.; Jeon, N. J.; Kim, Y. C.; Lee, D. U.; Shin, S. S.; Seo, J.; Kim, E. K.; Noh, J. H.; et al. Iodide Management in Formamidinium-Lead-Halide−Based Perovskite Layers for Efficient Solar Cells. *Science* **2017**, *356*, 1376−1379.

(2) Cai, M.; Wu, Y.; Chen, H.; Yang, X.; Qiang, Y.; Han, L. Cost-Performance Analysis of Perovskite Solar Modules. *Adv. sci.* **2017**, *4*, 1600269.

(3) Hong, W. L.; Huang, Y. C.; Chang, C. Y.; Zhang, Z. C.; Tsai, H. R.; Chang, N. Y.; Chao, Y. C. Efficient Low-Temperature Solution-Processed Lead-Free Perovskite Infrared Light-Emitting Diodes. *Adv. Mater.* **2016**, *28*, 8029−8036.

(4) Zhang, W.; Eperon, G. E.; Snaith, H. J. Metal Halide Perovskites for Energy Applications. *Nature Energy* **2016**, *1*, 16048.

(5) Zhang, X.; Lin, H.; Huang, H.; Reckmeier, C.; Zhang, Y.; Choy, W. C.; Rogach, A. L. Enhancing the Brightness of Cesium Lead Halide Perovskite Nanocrystal Based Green Light-Emitting Devices through the Interface Engineering with Perfluorinated Ionomer. *Nano Lett.* **2016**, *16*, 1415−1420.

(6) Bisquert, J.; Garcia-Belmonte, G.; Guerrero, A. Impedance Characteristics of Hybrid Organometal Halide Perovskite Solar Cells. *Springer International Publishing Switzerland* **2016**, 163−199.

(7) Flora, G.; Gupta, D.; Tiwari, A. Toxicity of Lead: A review with Recent Updates. *Interdiscip. Toxicol.* **2012**, *5*, 47−58.

(8) Shockley, W.; Queisser, H. J. Detailed Balance Limit of Efficiency of p-n Junction Solar Cells. *J. Appl. Phys.* **1961**, *32*, 510−519.

(9) Rühle, S. Tabulated Values of the Shockley−Queisser Limit for Single Junction Solar Cells. *Sol. Energy* **2016**, *130*, 139−147.

(10) Ogomi, Y.; Morita, A.; Tsukamoto, S.; Saitho, T.; Fujikawa, N.; Shen, Q.; Toyoda, T.; Yoshino, K.; Pandey, S. S.; Ma, T.; et al. $CH_3NH_3Sn_xPb_{(1-x)}I_3$ Perovskite Solar Cells Covering up to 1060 nm. *J. Phys. Chem. Lett.* **2014**, *5*, 1004−1011.

(11) Hao, F.; Stoumpos, C. C.; Cao, D. H.; Chang, R. P. H.; Kanatzidis, M. G. Lead-Free Solid-State Organic−Inorganic Halide Perovskite Solar Cells. *Nat. Photonics* **2014**, *8*, 489−494.

(12) Noel, N. K.; Stranks, S. D.; Abate, A.; Wehrenfennig, C.; Guarnera, S.; Haghighirad, A.-A.; Sadhanala, A.; Eperon, G. E.; Pathak, S. K.; Johnston, M. B.; et al. Lead-Free Organic-Inorganic Tin Halide Perovskites for Photovoltaic Applications. *Energy Environ. Sci.* **2014**, *7*, 3061−3068.

(13) Ergen, O.; Gilbert, S. M.; Pham, T.; Turner, S. J.; Tan, M. T. Z.; Worsley, M. A.; Zettl, A. Graded Bandgap Perovskite Solar Cells. *Nat. Mater.* **2016**, *16*, 522−525.

(14) Yokoyama, T.; Cao, D. H.; Stoumpos, C. C.; Song, T. B.; Sato, Y.; Aramaki, S.; Kanatzidis, M. G. Overcoming Short-Circuit in Lead-Free $CH_3NH_3SnI_3$ Perovskite Solar Cells via Kinetically Controlled Gas-Solid Reaction Film Fabrication Process. *J. Phys. Chem. Lett.* **2016**, *7*, 776−782.

(15) Tsai, C.-M.; Wu, H.-P.; Chang, S.-T.; Huang, C.-F.; Wang, C.-H.; Narra, S.; Yang, Y.-W.; Wang, C.-L.; Hung, C.-H.; Diau, E. W.-G. Role of Tin Chloride in Tin-Rich Mixed-Halide Perovskites Applied as Mesoscopic Solar Cells with a Carbon Counter Electrode. *ACS Energy Lett.* **2016**, *1*, 1086−1093.

(16) Song, T.-B.; Yokoyama, T.; Aramaki, S.; Kanatzidis, M. G. Performance Enhancement of Lead-Free Tin-Based Perovskite Solar Cells with Reducing Atmosphere-Assisted Dispersible Additive. *ACS Energy Lett.* **2017**, *2*, 897−903.

(17) Ke, W.; Stoumpos, C. C.; Logsdon, J. L.; Wasielewski, M. R.; Yan, Y.; Fang, G.; Kanatzidis, M. G. TiO_2-ZnS Cascade Electron Transport Layer for Efficient Formamidinium Tin Iodide Perovskite Solar Cells. *J. Am. Chem. Soc.* **2016**, *138*, 14998−15003.

(18) Stoumpos, C. C.; Malliakas, C. D.; Kanatzidis, M. G. Semiconducting Tin and Lead Iodide Perovskites with Organic Cations: Phase Transitions, High Mobilities, and Near-Infrared Photoluminescent Properties. *Inorg. Chem.* **2013**, *52*, 9019−9038.

(19) Rajendra Kumar, G.; Kim, H.-J.; Karupannan, S.; Prabakar, K. Interplay between Iodide and Tin Vacancies in $CsSnI_3$ Perovskite Solar Cells. *J. Phys. Chem. C* **2017**, *121*, 16447−16453.

(20) Xu, P.; Chen, S.; Xiang, H.-J.; Gong, X.-G.; Wei, S.-H. Influence of Defects and Synthesis Conditions on the Photovoltaic Performance of Perovskite Semiconductor $CsSnI_3$. *Chem. Mater.* **2014**, *26*, 6068−6072.

(21) Tsai, C.-M.; Mohanta, N.; Wang, C.-Y.; Lin, Y.-P.; Yang, Y.-W.; Wang, C.-L.; Hung, C.-H.; Diau, E. W.-G. Formation of Stable Tin Perovskites Co-crystallized with Three Halides for Carbon-Based Mesoscopic Lead-Free Perovskite Solar Cells. *Angew. Chem., Int. Ed.* **2017**, *56*, 13819−13823.

(22) Konstantakou, M.; Stergiopoulos, T. A critical Review on Tin Halide Perovskite Solar Cells. *J. Mater. Chem. A* **2017**, *5*, 11518−11549.

(23) Shao, S.; Liu, J.; Portale, G.; Fang, H.-H.; Blake, G. R.; ten Brink, G. H.; Koster, L. J. A.; Loi, M. A. Highly Reproducible Sn-Based Hybrid Perovskite Solar Cells with 9% Efficiency. *Adv. Energy Mater.* **2018**, *8*, 1702019.

(24) Liao, Y.; Liu, H.; Zhou, W.; Yang, D.; Shang, Y.; Shi, Z.; Li, B.; Jiang, X.; Zhang, L.; Quan, L. N.; et al. Highly Oriented Low-Dimensional Tin Halide Perovskites with Enhanced Stability and Photovoltaic Performance. *J. Am. Chem. Soc.* **2017**, *139*, 6693−6699.

(25) Ke, W.; Stoumpos, C. C.; Zhu, M.; Mao, L.; Spanopoulos, I.; Liu, J.; Kontsevoi, O. Y.; Chen, M.; Sarma, D.; Zhang, Y.; et al. Enhanced Photovoltaic Performance and Stability with a New Type of Hollow 3D Perovskite {en}$FASnI_3$. *Sci. Adv.* **2017**, *3*, e1701293.

(26) Ke, W.; Stoumpos, C. C.; Spanopoulos, I.; Mao, L.; Chen, M.; Wasielewski, M. R.; Kanatzidis, M. G. Efficient Lead-Free Solar Cells Based on Hollow {en}$MASnI_3$ Perovskites. *J. Am. Chem. Soc.* **2017**, *139*, 14800−14806.

(27) Cao, D. H.; Stoumpos, C. C.; Yokoyama, T.; Logsdon, J. L.; Song, T.-B.; Farha, O. K.; Wasielewski, M. R.; Hupp, J. T.; Kanatzidis, M. G. Thin Films and Solar Cells Based on Semiconducting Two-Dimensional Ruddlesden−Popper $(CH_3(CH_2)_3NH_3)_2(CH_3NH_3)_{n-1}Sn_nI_{3n+1}$ Perovskites. *ACS Energy Lett.* **2017**, *2*, 982−990.

(28) Mercier, N.; Poiroux, S.; Riou, A.; Batail, P. Unique Hydrogen Bonding Correlating with a Reduced Band Gap and Phase Transition in the Hybrid Perovskites $(HO(CH_2)_2NH_3)_2PbX_4$ (X = I, Br). *Inorg. Chem.* **2004**, *43*, 8361−8366.

(29) Tsai, C.-M.; Wu, G.-W.; Narra, S.; Chang, H.-M.; Mohanta, N.; Wu, H.-P.; Wang, C.-L.; Diau, E. W.-G. Control of Preferred Orientation with Slow Crystallization for Carbon-Based Mesoscopic Perovskite Solar Cells Attaining Efficiency 15%. *J. Mater. Chem. A* **2017**, *5*, 739−747.

(30) Leblanc, A.; Allain, M.; Dittmer, J.; Fernandez, V.; Pauporte, T.; Mercier, N. Lead- and Iodide-Deficient $(CH_3NH_3)PbI_3$ (d-MAPI): The Bridge between 2D and 3D Hybrid Perovskites. *Angew. Chem., Int. Ed.* **2017**, *56*, 16067−16072.

(31) Chan, C.-Y.; Wang, Y.; Wu, G.-W.; Diau, E. W.-G. Solvent-Extraction Crystal Growth for Highly Efficient Carbon-Based Mesoscopic Perovskite Solar Cells Free of Hole Conductors. *J. Mater. Chem. A* **2016**, *4*, 3872−3878.

(32) Jokar, E.; Chien, C.-H.; Fathi, A.; Rameez, M.; Chang, Y.-H.; Diau, E. W.-G. Slow Surface Passivation and Crystal Relaxation with Additives to Improve Device Performance and Durability for Tin-Based Perovskite Solar Cells. *Energy Environ. Sci.* **2018**, DOI: 10.1039/C8EE00956B.

(33) Walsh, A. Principles of Chemical Bonding and Band Gap Engineering in Hybrid Organic-Inorganic Halide Perovskites. *J. Phys. Chem. C* **2015**, *119*, 5755−5760.

(34) Endres, J.; Egger, D. A.; Kulbak, M.; Kerner, R. A.; Zhao, L.; Silver, S. H.; Hodes, G.; Rand, B. P.; Cahen, D.; Kronik, L.; et al. Valence and Conduction Band Densities of States of Metal Halide Perovskites: A Combined Experimental-Theoretical Study. *J. Phys. Chem. Lett.* **2016**, *7*, 2722−2729.

(35) He, Y.; Galli, G. Perovskites for Solar Thermoelectric Applications: A First Principle Study of $CH_3NH_3AI_3(A = Pb$ and Sn). *Chem. Mater.* **2014**, *26*, 5394−5400.

(36) Brivio, F.; Walker, A. B.; Walsh, A. Structural and Electronic Properties of Hybrid Perovskites for High-Efficiency Thin-Film Photovoltaics from First-Principles. *APL Mater.* **2013**, *1*, 042111.

(37) Prasanna, R.; Gold-Parker, A.; Leijtens, T.; Conings, B.; Babayigit, A.; Boyen, H. G.; Toney, M. F.; McGehee, M. D. Band Gap Tuning via Lattice Contraction and Octahedral Tilting in Perovskite Materials for Photovoltaics. *J. Am. Chem. Soc.* **2017**, *139*, 11117−11124.

(38) Chung, C.-C.; Narra, S.; Jokar, E.; Wu, H.-P.; Diau, E. W.-G. Inverted Planar Solar Cells Based on Perovskite/Graphene Oxide Hybrid Composites. *J. Mater. Chem. A* **2017**, *5*, 13957−13965.

(39) Wang, B.; Wong, K. Y.; Yang, S.; Chen, T. Crystallinity and Defect State Engineering in Organo-Lead Halide Perovskite for High-Efficiency Solar Cells. *J. Mater. Chem. A* **2016**, *4*, 3806−3812.

(40) Shi, D.; Adinolfi, V.; Comin, R.; Yuan, M.; Alarousu, E.; Buin, A.; Chen, Y.; Hoogland, S.; Rothenberger, A.; Katsiev, K.; et al. Low Trap-State Density and Long Carrier Diffusion in Organolead Trihalide Perovskite Single Crystals. *Science* **2015**, *347*, 519−522.

■ NOTE ADDED AFTER ASAP PUBLICATION

This paper published ASAP on August 13, 2018 with incomplete Supporting Information files. The corrected paper reposted to the Web on August 16, 2018.